



Synergistic Effect of Cation and Anion for Low-Temperature Aqueous Zinc-Ion Battery

Cite as

Nano-Micro Lett.

(2021) 13:204

Tianjiang Sun¹, Shibing Zheng¹, Haihui Du¹, Zhanliang Tao¹ ✉

Received: 13 July 2021

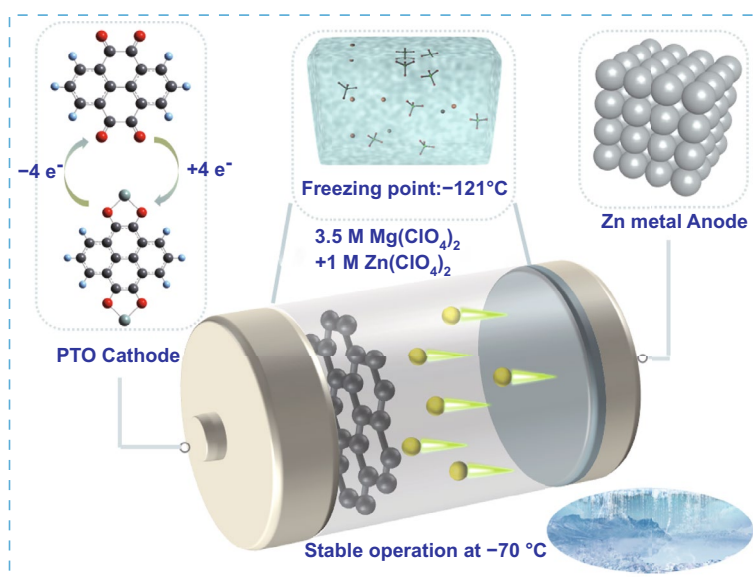
Accepted: 8 September 2021

© The Author(s) 2021

HIGHLIGHTS

- The ratio of hydrogen bonds in water molecules is significantly decreased by introducing oxygen-ligand Mg^{2+} and hydrogen-ligand ClO_4^- , resulting in an ultralow solidifying point of -121°C .
- The excellent low-temperature physicochemical properties and good compatibility with Zn metal of $3.5\text{ M (mol L}^{-1}\text{) Mg(ClO}_4\text{)}_2 + 1\text{ M Zn(ClO}_4\text{)}_2$ electrolyte gives fabricated Zn||pyrene-4,5,9,10-tetraone (PTO) battery and Zn||Phenazine (PNZ) battery a satisfactory low temperature performance.

ABSTRACT Although aqueous zinc-ion batteries have gained great development due to their many merits, the frozen aqueous electrolyte hinders their practical application at low temperature conditions. Here, the synergistic effect of cation and anion to break the hydrogen-bonds network of original water molecules is demonstrated by multi-perspective characterization. Then, an aqueous-salt hydrates deep eutectic solvent of $3.5\text{ M Mg(ClO}_4\text{)}_2 + 1\text{ M Zn(ClO}_4\text{)}_2$ is proposed and displays an ultralow freezing point of -121°C . A high ionic conductivity of 1.41 mS cm^{-1} and low viscosity of 22.9 mPa s at -70°C imply a fast ions transport behavior of this electrolyte. With the benefits of the low-temperature electrolyte, the fabricated Zn||Pyrene-4,5,9,10-tetraone (PTO) and Zn||Phenazine (PNZ) batteries exhibit satisfactory low-temperature performance. For example, Zn||PTO battery shows a high discharge capacity of 101.5 mAh g^{-1} at 0.5 C (200 mA g^{-1}) and 71 mAh g^{-1} at 3 C (1.2 A g^{-1}) when the temperature drops to -70°C . This work provides an unique view to design anti-freezing aqueous electrolyte.



✉ Zhanliang Tao, taozhl@nankai.edu.cn

¹ Key Laboratory of Advanced Energy Materials Chemistry (Ministry of Education), Renewable Energy Conversion and Storage Center, College of Chemistry, Nankai University, Tianjin 300071, People's Republic of China

KEYWORDS Low-temperature aqueous zinc-ion battery; 3.5 M $\text{Mg}(\text{ClO}_4)_2$ + 1 M $\text{Zn}(\text{ClO}_4)_2$ electrolyte; Synergistic effect; Pyrene-4,5,9,10-tetraone; Phenazine

1 Introduction

The temperature in surface of earth is unevenly, which results in a great challenge for energy storage devices. For example, there are abundant wind and solar in severe cold regions, but how to store these energies becomes a problem. Aqueous zinc-ion batteries (AZIBs), with merits of high theoretical specific capacity and low redox potential of Zn anode, low cost and high ionic conductivity of aqueous electrolyte, and various cathode materials, have attracted tremendous attention from researchers and have shown great potential for large-scale energy storage devices [1–6]. Unfortunately, AZIBs show terrible electrochemical performance at low-temperature condition, which hinders their application in harsh environments. For AZIBs, the ultralow and ultrahigh activation energies of the anodic and cathodic reactions result in insensitive electrode kinetics to varied temperatures based on the Arrhenius Equation [7]. While the aqueous electrolytes are extremely sensitive to temperature. As we know, the thermodynamic freezing point of solvent water is 0 °C. When temperature further drops, the aqueous electrolyte will freeze, and the ionic conductivity and interface wettability will rapidly deteriorate, which causes AZIBs cannot work normally [8, 9]. Therefore, inhibition of aqueous electrolyte freezing is an effective strategy to improve the low-temperature performance of AZIBs.

The formation of ice crystal is driven by hydrogen bonds (HBs) between water molecules [9, 10]. Modulating the chemical environment of O and H atoms in water to break the HBs network is possible to induce the freezing point depression of water. To date, several strategies have been reported including hybrid electrolyte with cosolvents or antisolvent additives, high-concentration electrolyte, and hydrogel electrolyte, etc. [11–16]. Although these methods improve the low-temperature performance of AZIBs to some extent, some inherent problems still hinder their practical application, such as low ionic conductivity and environmental unfriendliness of organic additives, high viscosity, and cost of high-concentration salt, and complex synthesis and assembly processes of hydrogel electrolyte. Essentially, these strategies alter coordination environment of H atoms

by introducing HBs acceptors and further lower its freezing point. The researches about adjust chemical environment of O atoms to suppress ice up are ignored, which are worthy of further study.

Deep eutectic solvents (DES), as a kind of “green” solvent, have been studied to protect the Zn metal anode for AZIBs [17–19]. Meanwhile, it also exhibits a certain anti-freezing property due to the interaction with water molecules. However, conventional DES systems (for example, aqueous-organic DES mixture) commonly show low ionic conductivity and high viscosity at low temperature due to the low water content. In contrast, the aqueous-salt hydrates DES, without organic compound, is worth to be considered for application in low-temperature AZIBs. Aqueous-salt hydrates possess rich hydrogen-bond (HB) acceptor and hydrogen-bond donor, which effectively destroy the HBs network of original water molecules [20, 21]. By simultaneously regulating the coordination environment of O and H atoms in water, this DES system can obtain a low freezing point.

Here, an anti-freezing dual-cations EDS electrolyte of 3.5 M (mol L^{-1}) $\text{Mg}(\text{ClO}_4)_2$ + 1 M $\text{Zn}(\text{ClO}_4)_2$ is reported for low-temperature AZIBs. It is discovered that the ratio of HBs in water molecules is significantly decreased by introducing oxygen-ligand Mg^{2+} and hydrogen-ligand ClO_4^- , resulting in an ultralow solidifying point of –121 °C. The novel aqueous-salt hydrate shows high ionic conductivity, low viscosity, and activation energy at –70 °C due to the absence of organic additive. The excellent low-temperature physicochemical properties and good compatibility with Zn metal of this electrolyte give fabricated Zn||pyrene-4,5,9,10-tetraone (PTO) battery and Zn||Phenazine (PNZ) battery a satisfactory low temperature performance. For example, when at –70 °C, the Zn||PTO battery exhibits a high discharge capacity of 101.5 mAh g^{-1} at 0.5 C (200 mA g^{-1}) and excellent rate performance (71 mAh g^{-1} at 3 C (1.2 A g^{-1})).

2 Experimental Section

2.1 Preparation of Pyrene-4,5,9,10-tetraone (PTO) Sample

Pyrene-4,5,9,10-tetraone (PTO) was prepared by a previously reported method. 8.08 g pyrene was added into 160 mL CH_2Cl_2 and 160 mL acetonitrile, followed by adding 72 g

NaIO_4 , 200 mL H_2O , and 1.0 g $\text{RuCl}_3 \cdot x\text{H}_2\text{O}$ successively. The mixture was heated at 45 °C overnight and then organic solvents of which were filtrated and washed with CH_2Cl_2 several times. Obtained filtrate was further washed with H_2O and CH_2Cl_2 and removed by rotary evaporation treatment. The pure golden needle-like product PTO was obtained going through column chromatography (using CH_2Cl_2 as mobile phase).

2.2 Material Characterizations

DSC (NETZSCH, TG209 DSC204 DMA242 TMA202) was carried out in the procedure of +25 ~ -150 °C with a cooling rate of 5 °C min^{-1} and scanned from -150 to +25 °C at 5 °C min^{-1} . The polarizing microscope was using Olympus BX51TRF, liquid nitrogen as refrigerant, and the cooling rate was 4 °C min^{-1} and standing 10 min at specific temperature. The viscosity of electrolytes was tested by Rotary viscometer (Ji Chang, NDJ-8S), and anhydrous ethanol was used as refrigerant. The characteristics of electrolyte were conducted by Raman spectroscopy (Renishaw, InVia Reflex microscope with 532 nm excitation laser, 100 ~ 4000 cm^{-1}) and Fourier transform infrared spectroscopy (FTIR, BRUKER TENSOR II (FTS6000), 400 ~ 4000 cm^{-1}). ^1H NMR analysis was carried out on an AVANCE III 400 MHz equipment. The morphologies and structures of the PTO were examined by scanning electron microscopy (SEM, JEOL JSM-7500F) and X-ray diffraction (XRD, Rigaku SmartLab 9 KW, Cu $K\alpha$ radiation). All low-temperature tested were performed at ultra-low-temperature storage box (MELNG, DW-HW50).

2.3 Electrochemical Measurement

The PTO and PNZ electrodes are prepared by mixing PTO or PNZ, Ketjen black (KB), and polytetrafluoroethylene (PTFE) at an appropriate weight ratio of 5:4:1 and are pressed onto stainless-steel mesh (Φ 12 mm). Then, the electrode films are dried at 80 °C for 12 h under vacuum. The active materials mass loading is 1–2 mg cm^{-2} . The 2032-type coin cells are assembled by PTO or PNZ cathode, 3.5 M $\text{Mg}(\text{ClO}_4)_2 + 1 \text{ M Zn}(\text{ClO}_4)_2$ electrolyte, Zn metal (0.05 mm, Φ 12 mm) anode and glass fiber separator. CV tests are carried out on an electrochemical workstation (CHI660E). The galvanostatic charge/discharge tests are implemented after

resting 5 h by using a battery test system (LAND CT2001A). The tested voltage range of Zn||PTO is 0.3 ~ 1.5 V (vs. Zn^{2+}/Zn). The tested voltage range of Zn||PNZ is 0.3 ~ 1.5 and 0.2 ~ 1.5 V (vs. Zn^{2+}/Zn) at 25 and -70 °C, respectively. The current density and specific capacity of full battery are based on the active mass of cathode in each electrode. The ionic conductivity is tested by fabricated coin cell, which includes filled electrolyte, cathode, and anode stainless-steel case (Φ 20 mm).

2.4 Calculation Details

The ionic conductivity is calculated follow Eq. 1:

$$\sigma = \frac{L}{RS} \quad (1)$$

σ : Ionic conductivity; L : thicknesses of the electrolyte (0.3 cm); R : resistance of the electrolyte; S : area of the electrolyte (3.14 cm^2).

The activation energy is calculated follow Eqs. 2 and 3:

$$\sigma = \frac{A}{T} e^{-\frac{E_a}{Tk}} \quad (2)$$

$$\ln(\sigma T) = \ln(A) - \frac{E_a}{kT} \quad (3)$$

σ : Ionic conductivity; T : temperature; E_a : activation energy; k : Boltzmann constant ($1.3807 \times 10^{-23} \text{ J K}^{-1}$). The $-E_a/k$ was fitted by different temperature $\ln(\sigma T)$ and $1/T$. The E_a was obtained.

2.5 DFT Calculation

All of the calculations are carried out using the Gaussian 16 program. Geometry optimization and frequency analysis are performed in water solvent with the SMD solvation model. C, H, O, N using B3LYP functional and 6-31+G (d, p) basis set. Zn^{2+} and Mg^{2+} using B3LYP functional and def2tzvp basis set.

3 Results and Discussion

3.1 Synergistic Effect of Mg^{2+} and ClO_4^-

As mentioned above, it is a key that finding suitable salt to construct anti-freezing aqueous-salt hydrates EDS



electrolyte. Aqueous electrolytes are constituted by various anions and cations. Matching type of anion and cation can simultaneously modulate the chemical environment of O and H atoms of H₂O. Anions, such as BF₄⁻, Cl⁻, and CF₃SO₃⁻, can form weak HBs with water molecules to suppress ice up of water [8–10, 22, 23]. Besides, ClO₄⁻, as a kind of chaotropic anion, also has ability to form a lot of HBs with water molecules due to contain four HBs-acceptor O atoms [24–26]. Cations commonly exist in aqueous electrolyte in the form of hydration [27, 28]. Among of various divalent cations, Mg²⁺ with smaller ionic radius (0.72 nm) and concentrated surface charge density displays strong electrostatic attraction with O atom of H₂O. Thus, aqueous-Mg(ClO₄)₂ salt solution shows satisfactory anti-freezing ability at a certain concentration.

Firstly, the hydrated interactions of Mg²⁺ and Zn²⁺ are investigated by density functional theory (DFT) calculations. As shown in Fig. 1a, b, the solvation configurations of Mg²⁺ and Zn²⁺ with six water molecules are simulated. The hydrated radius of Mg(H₂O)₆²⁺ (2.1 Å) is smaller than Zn(H₂O)₆²⁺ (2.2 Å). In addition, the binding energy of Mg(H₂O)₆²⁺ is -4.14 eV, which is obviously lower than

Zn(H₂O)₆²⁺ (-1.72 eV and H₂O-H₂O (-0.13 eV, Fig. S1). The result indicates that the Mg²⁺ has stronger interaction with O atom of H₂O, which can hinder the formation of HBs network by competing with the H of H₂O. Fourier transform infrared spectroscopy (FTIR) is utilized to observe the change of HBs in different electrolytes. As shown in Fig. S2a, the peaks at 2900~3700 cm⁻¹ correspond to O-H stretching vibration of H₂O [29]. Notably, the intensity of high-wavenumber peak in 1 M Mg(ClO₄)₂ solution is increased in comparison with that in 1 M Zn(ClO₄)₂ solution. While the stretching vibration of Cl-O at 1093 cm⁻¹ has no shift (Fig. S2b) [30]. The peaks of O-H stretching vibration are further divided into three components, corresponding to strong HBs, medium HBs, and weak HBs, respectively (Fig. S3). As detected, the ratio of weak HBs in 1 M Mg(ClO₄)₂ solution is higher than that in 1 M Zn(ClO₄)₂ solution, suggesting that Mg²⁺ has stronger ability to break HBs network of water molecules (Fig. S4). The ¹H nuclear magnetic resonance (¹H NMR) also confirms reduced HBs effect of water molecules and content of free water in 1 M Mg(ClO₄)₂ solution (Fig. S5). In addition, the dissolution Mg(ClO₄)₂ salt in water is a violent exothermic process,

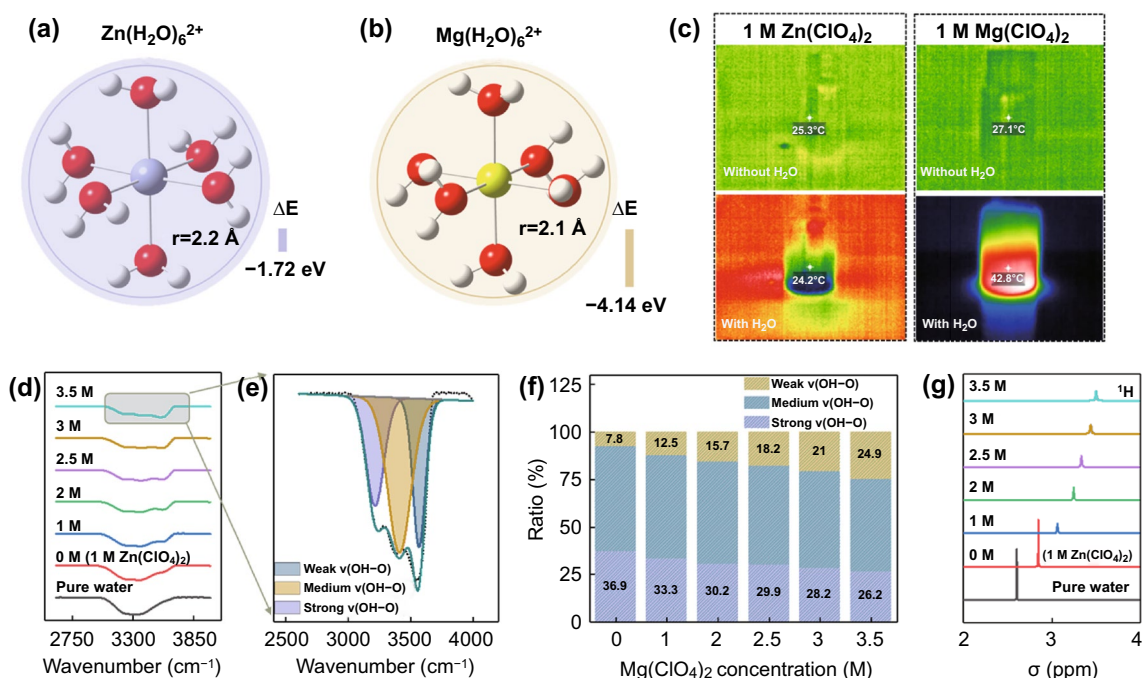


Fig. 1 The calculated formation energy and hydrated radius of **a** Zn²⁺ solvation configuration. **b** Mg²⁺ solvation configuration. **c** Photographs of infrared thermometry of different electrolytes. **d** FTIR spectra for O-H bond. **e** The fitted O-H stretching vibration representing the strong, medium weak OH···O HBs. **f** The ratio of different types of HBs. **g** ¹H NMR spectra of different concentration electrolytes

which implies the bond-formation energy between Mg^{2+} and O atoms is higher than bond-cleavage energy of HBs (Fig. 1c). Thus, Mg^{2+} is easier to combine with O atoms in H_2O and breaks up the hydrogen-bond arrangement. Thus, the freezing point of 1 M $\text{Mg}(\text{ClO}_4)_2$ solution is lower than 1 M $\text{Zn}(\text{ClO}_4)_2$ solution (Fig. S6).

The interaction between anion and water molecules is systematically investigated by spectroscopic methods. The FTIR spectra of O–H stretching vibration for different concentration electrolytes are collected and summarized in Figs. 1d and S7 (x M: x M $\text{Mg}(\text{ClO}_4)_2 + 1$ M $\text{Zn}(\text{ClO}_4)_2$). As shown in Figs. 1d, e and S8, the fitting peaks of strong and medium HBs gradually weaken and shift to high wavenumber (blue shift) with increasing concentration of $\text{Mg}(\text{ClO}_4)_2$. On the contrary, the weak HBs peak gradually enhances and shifts to low wavenumber (red shift). DFT calculations show that the bond length of O–H in H_2O (0.982 Å) is longer when forming weak HBs with ClO_4^- (0.970 Å) (Fig. S9), thus resulting in the peaks of strong and medium HBs have blue shift (Fig. S8). Meanwhile, the ratio of weak HBs is increased (Fig. 1f). In addition, the Cl–O stretching vibration at about 1093 cm^{-1} has a red shift (Fig. S10), which

is consistent with DFT calculations (Fig. S9, the bond length of Cl–O is getting longer). Raman spectra of aqueous-salt hydrates with different concentration $\text{Mg}(\text{ClO}_4)_2$ are collected. As shown in Fig. S11, the wide peak at $3000\sim 3700\text{ cm}^{-1}$ is attribute to O–H stretching vibration, which is constituted with three type HBs [31]. Similarly, the strong and medium HBs peaks have blue shift, and weak HBs shifts to low wavenumber with the increasing concentration, and the HBs ratio of $\text{H}_2\text{O}\text{--}\text{H}_2\text{O}$ has obvious decrease (Fig. S12). ^1H NMR is performed to study the HBs network in this system. As shown in Figs. 1g and S13, it can be seen that the ^1H chemical site shifts to low field with increasing concentration of $\text{Mg}(\text{ClO}_4)_2$, which is caused by reduced electron cloud density of H in H_2O when formed weak $\text{ClO}_4^- \text{--}\text{H}_2\text{O}$ HBs (Figs. S1 and S9, the Mulliken charge of H in $\text{ClO}_4^- \text{--}\text{H}_2\text{O}$ is lower than in $\text{H}_2\text{O}\text{--}\text{H}_2\text{O}$). DFT and spectroscopic results demonstrate that ClO_4^- has ability to form weak HBs with water molecules and depresses HBs network formation among of water molecules. Benefitting from synergistic effect of cation and anion, the aqueous- $\text{Mg}(\text{ClO}_4)_2/\text{Zn}(\text{ClO}_4)_2$ DES system has satisfactory anti-freeze potential in theory.

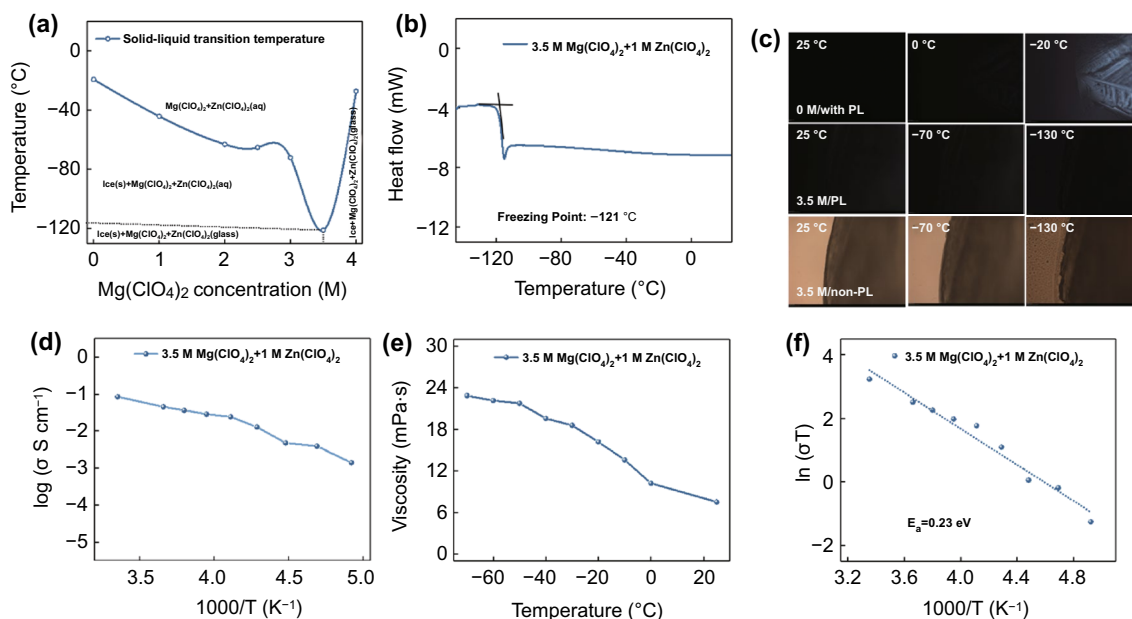


Fig. 2 **a** V-shape relationship between the freezing temperature and concentration of $\text{Mg}(\text{ClO}_4)_2$ (0 M refers to 1 M $\text{Zn}(\text{ClO}_4)_2$). **b** DSC curve of 3.5 M electrolyte. **c** Polarizing light (PL) and non-polarizing light microscope observation of 0 M and 3.5 M electrolyte. **d** Ionic conductivity of 3.5 M electrolyte at different temperatures. **e** Viscosity of 3.5 M electrolyte at different temperatures. **f** Electric conductance activation energy of 3.5 M electrolyte

3.2 Low-Temperature Properties of 3.5 M Electrolyte

The freezing points of different concentration solution are tested by differential scanning calorimetry (DSC) (Fig. S14). Figure 2a shows the V-shape relationship between the liquid–solid transition temperature and concentration of $\text{Mg}(\text{ClO}_4)_2$. When the concentration of $\text{Mg}(\text{ClO}_4)_2$ increases to 3.5 M, an ultralow glass transition temperature of $-121\text{ }^\circ\text{C}$ is obtained (Fig. 2b) [32]. The freezing temperature below 3.5 M is mainly dominated by HBs ratio among of water molecules. However, above 3.5 M, the freezing temperature is raised because of increased ions interaction [9]. Therefore, 3.5 M $\text{Mg}(\text{ClO}_4)_2 + 1\text{ M Zn}(\text{ClO}_4)_2$ (3.5 M) solution can be used as electrolyte for low-temperature AZIBs. In situ polarizing light (PL) or non-PL microscope is applied to intuitively observe solidification state of different electrolytes. As shown in Fig. 2c, under PL, the 0 M electrolyte (1 M $\text{Zn}(\text{ClO}_4)_2$) shows clear ice crystal birefringence when temperature drops to $-20\text{ }^\circ\text{C}$. However, no signal is detected for 3.5 M electrolyte (3.5 M $\text{Mg}(\text{ClO}_4)_2 + 1\text{ M Zn}(\text{ClO}_4)_2$) even at $-130\text{ }^\circ\text{C}$, due to the fact that glass transition corresponds to the formation of the amorphous phase. Under non-PL, the crystalline state of 0 M electrolyte at $-20\text{ }^\circ\text{C}$ is clearly observed (Fig. S15). By contrast, the 3.5 M electrolyte still maintains liquid state at $-70\text{ }^\circ\text{C}$, and an uneven boundary appears when temperature reduces to $-130\text{ }^\circ\text{C}$, indicating the solution transforms into brittle glass (Fig. 2c). Thus, 3.5 M solution shows a good freezing resistance and its physicochemical properties are further investigated. The ionic conductivity of 3.5 M electrolyte at different temperature from $+25\text{ }^\circ\text{C}$ to $-70\text{ }^\circ\text{C}$ is calculated by impedance of electrolyte. As shown in Fig. 2d, it shows a high ionic conductivity of 1.41 mS cm^{-1} at $-70\text{ }^\circ\text{C}$. A low viscosity of 22.9 mPa s is achieved at $-70\text{ }^\circ\text{C}$, which enables fast ion transport (Fig. 2e). The conductive activation energy (E_a) of 3.5 M electrolyte is fitted by the relationship between ionic conductivity and temperature (Fig. 2f). The E_a is calculated to be 0.23 eV , implying fast ions diffusion ability. The excellent physicochemical properties enable AZIBs to achieve a favorable low-temperature performance.

3.3 Compatibility Between 3.5 M Electrolyte and Zn Anode

The compatibility between 3.5 M electrolyte and Zn metal anode is further understood. It is well known that introduced metal cations in AZIBs electrolyte can promote uniform deposition Zn and alleviate its dendrite problem by electrostatic shield effect [33–35]. The Mg^{2+} has concentrated surface charges on account of small ionic radius (0.72 nm) and high positive charge. Thus, the Mg^{2+} has more distinct electrostatic shield effect than univalent cation in theory. The cyclic voltammetry (CV) curves Fig. S16a show excellent reversibility of Zn plating/stripping on stainless-steel mesh (SS) in 3.5 M electrolyte. Compared with 0 M electrolyte (1 M $\text{Zn}(\text{ClO}_4)_2$ electrolyte), the Zn||SS half cell shows smaller voltage polarization in 3.5 M electrolyte (Fig. S16b). An obvious Zn plating peak (wide peak, not sharp peak) in 3.5 M electrolyte is detected, implying a depression of side reaction. In addition, the symmetric Zn||Zn battery in 3.5 M electrolyte exhibits a long-term cycling life of 500 h with a low and stable voltage polarization of 50 mV at 0.5 mA cm^{-2} . While in 0 M electrolyte (1 M $\text{Zn}(\text{ClO}_4)_2$), the symmetric battery shows increased voltage polarization and finally shorted circuit at about 450 h (Fig. S17). The symmetric Zn||Zn battery also displays excellent cycling stability at 1 mA cm^{-2} (Fig. S18). Scanning electron microscopy (SEM) image shows compact and smooth Zn surface after cycling 10 times at 3.5 M electrolyte (Fig. S19). These results suggest Mg^{2+} has significant protect effect for Zn plating process, showing the potential feasibility of applying 3.5 M electrolyte for AZIBs.

3.4 Reaction Mechanism of PTO and PNZ Electrodes

To fabricate a high-performance low-temperature AZIBs, suitable electrode materials are selected. Organic electrode materials, with many advantages such as low cost, environmentally friendly, fast reaction kinetics, and high capacity independence of temperature, have been seen as a feasible choose [36–38]. Thus, pyrene-4,5,9,10-tetraone

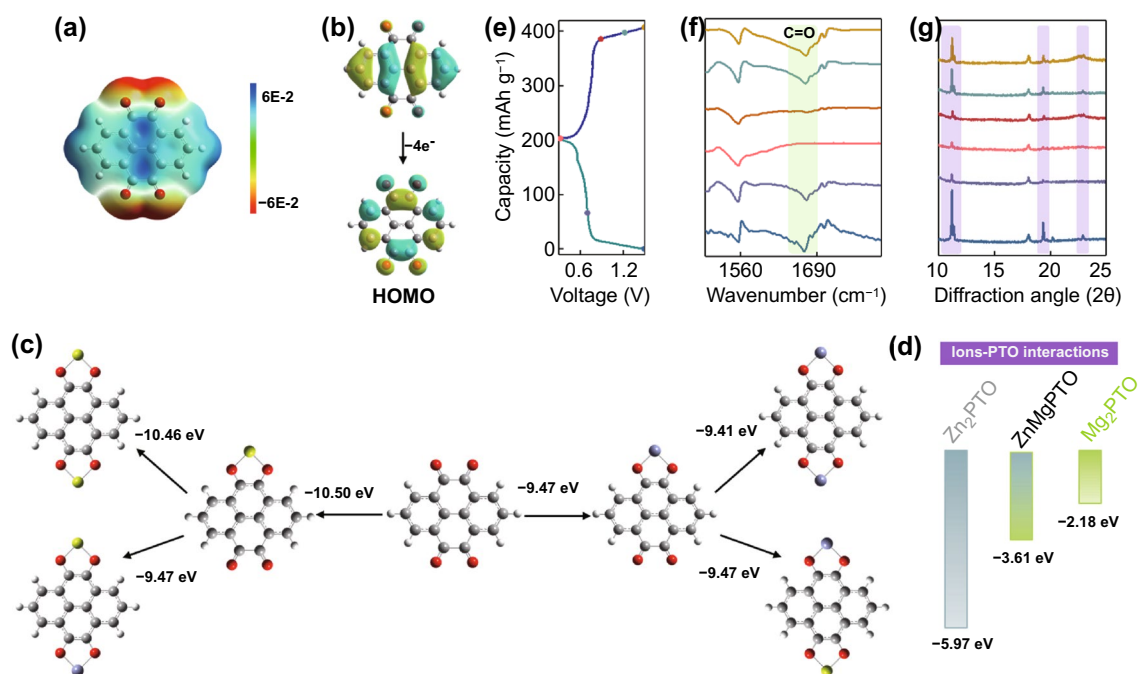


Fig. 3 **a** ESP of PTO molecule. **b** HOMO plots of PTO and PTO^{4-} . **c** Binding energies between PTO and Zn^{2+} or Mg^{2+} . **d** The corrected binding energy levels of Zn_2PTO , ZnMgPTO , and Mg_2PTO . **e** Charge–discharge curves of $\text{Zn}||\text{PTO}$ battery. **f** Ex situ FTIR spectra of PTO electrodes. **g** Ex situ XRD patterns of PTO electrodes

(PTO) with electroactive carbonyl groups and phenazine (PNZ) with electroactive conjugated amino groups are selected to construct low-temperature AZIBs. It is worth noting that a great number of Mg^{2+} exist in this EDS electrolyte (3.5 M electrolyte), which may be involved in organic electrode reaction. To distinguish it, DFT calculations are firstly carried out. The negative electrostatic potential (ESP) of the carbonyl groups in PTO molecule in Fig. 3a reveals its reaction sites. As shown in Fig. 3b, the effective electron delocalization occurs in the conjugated structure when PTO is reduced PTO^{4-} with accepting four electrons, indicating it can occur to four-electron reduction [39]. Thus, the binding energy of two cations (Mg^{2+} or Zn^{2+}) one PTO molecule are calculated. As shown in Fig. 3c, the bind energy of PTO with two Mg^{2+} (-10.46 eV) is lower than with two Zn^{2+} (-9.41 eV), and it also is lower than ZnMgPTO (-9.47 eV). However, it cannot be ignored that the metal cation binding to PTO requires a de-solvation process. As mentioned above, the hydrated energy of Zn^{2+} (-1.72 eV) is higher than Mg^{2+} (-4.14 eV). The Mg^{2+} needs more energy to break the

interaction with H_2O molecules and then combine with PTO. Considering the de-solvation energy of metal cations, the bind energy of Zn_2PTO is re-calculated to be -5.97 eV, which is smaller than ZnMgPTO (-3.61 eV) and Mg_2PTO (-2.18 eV) (Fig. 3d), suggesting that the PTO tends to bind to Zn^{2+} not Mg^{2+} . In addition, the CV curves of $\text{Zn}||\text{PTO}$ battery in 3.5 M and 0 M electrolyte (1 M $\text{Zn}(\text{ClO}_4)_2$) show similar shape and potential, while it is different from in 3.5 M $\text{Mg}(\text{ClO}_4)_2$ electrolyte (Fig. S20). The result implies that the redox reaction of PTO is independent of Mg^{2+} . The PNZ also exhibits similar reaction mechanism by DFT calculations (Fig. S21). The reaction mechanism of PTO is further confirmed by ex situ FTIR and XRD patterns. As shown in Fig. 3f, the peak intensity of C=O groups shows a reversible weakening and enhancement during discharge and charge processes, suggesting that the C=O groups are the combining site of Zn^{2+} . Meanwhile, the diffraction peaks of PTO at 11.18° , 19.36° , and 22.92° have same change, indicating a good reversibility. Noted that, no other by-produce diffraction peaks are observed (for example, basic zinc sulfates), suggesting only Zn^{2+} participates in the

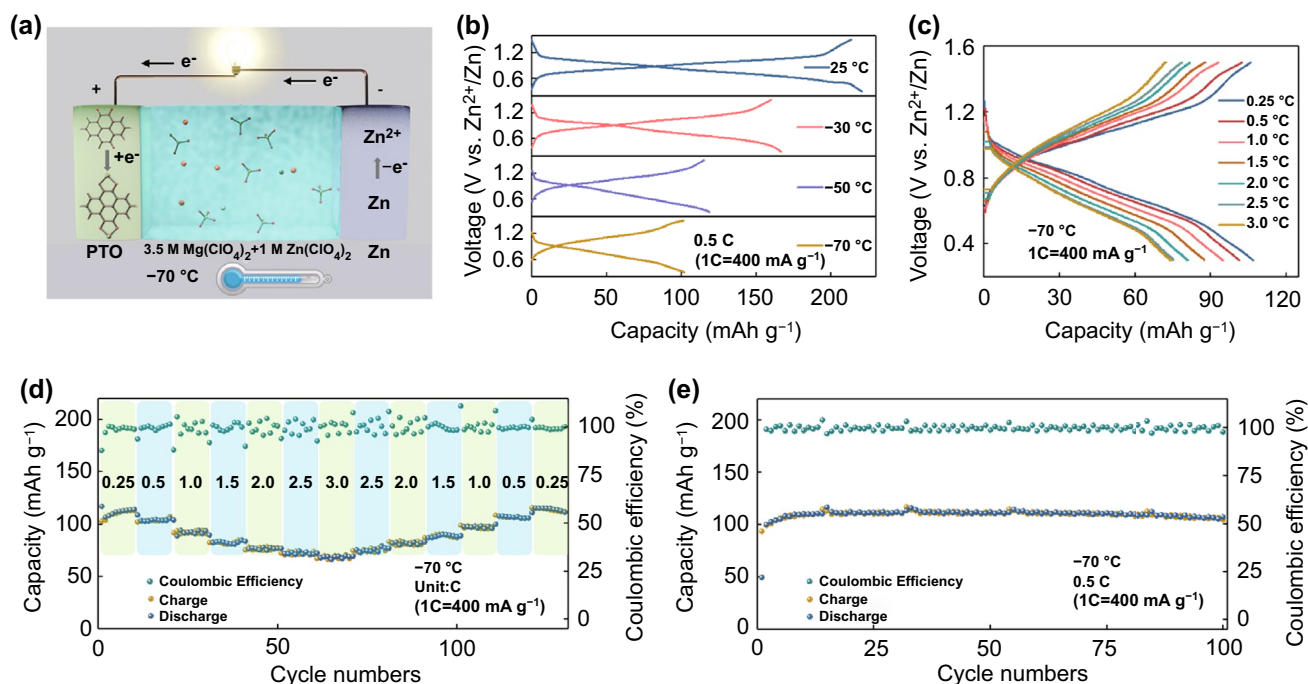


Fig. 4 **a** Schematic of low-temperature Zn||PTO battery. **b** Charge–discharge curves of Zn||PTO battery at different temperatures. **c** Charge–discharge curves of Zn||PTO battery at different current density. **d** Rate capacity of Zn||PTO battery at $-70\text{ }^{\circ}\text{C}$. **e** Cycling stability of Zn||PTO battery at $-70\text{ }^{\circ}\text{C}$

redox process. This conclusion can also be demonstrated by ex situ SEM images and energy-dispersive spectroscopy (EDS) (Fig. S22 and Table S1).

3.5 Low-Temperature Performance of Zn||PTO and Zn||PNZ Battery

The low-temperature AZIBs are constructed by $3.5\text{ M Mg}(\text{ClO}_4)_2 + 1\text{ M Zn}(\text{ClO}_4)_2$ electrolyte, PTO cathode, and Zn metal anode (Fig. 4a). The CV curves of Zn||PTO battery at $+25\text{ }^{\circ}\text{C}$ to $-70\text{ }^{\circ}\text{C}$ show a good reversibility (Fig. S23). The voltage polarization of Zn||PTO battery has gradually increased when temperature dropped, which may be caused by increased activation process of PTO material and concentration polarization of the electrolyte. Figure 4b shows the charge–discharge curves of Zn||PTO battery range from $+25\text{ }^{\circ}\text{C}$ to $-70\text{ }^{\circ}\text{C}$. It can work well at $-70\text{ }^{\circ}\text{C}$ and exhibit a high discharge capacity of 101.5 mAh g^{-1} at 200 mA g^{-1} . Even at ultrahigh current density of 3 C (1.2 A g^{-1}), this

system still maintains 71 mAh g^{-1} discharge capacity, which is 67% of the capacity at 100 mA g^{-1} (Fig. 4c). The discharge capacity recovers to initial level when current density increases to 0.25 C (100 mA g^{-1}). The excellent rate performance of Zn||PTO battery benefits from 3.5 M electrolyte with high ionic conductivity, low viscosity and activation energy at low temperature. As shown in Fig. 4e, the Zn||PTO battery also can cycle 100 times with no obvious capacity fading at $-70\text{ }^{\circ}\text{C}$ and achieve near 100% coulombic efficiency. In addition, the Zn||PNZ battery is fabricated and tested at $+25\text{ }^{\circ}\text{C}$ to $-70\text{ }^{\circ}\text{C}$. The CV curves of Zn||PNZ battery at $+25$ and $-70\text{ }^{\circ}\text{C}$ are displayed in Fig. S24. This system obtained discharge capacity of 218.7 and 115.6 mAh g^{-1} at $+25$ and $-70\text{ }^{\circ}\text{C}$, respectively (Fig. S25). The battery also shows a good rate capacity at $-70\text{ }^{\circ}\text{C}$. A high discharge capacity of 68.3 mAh g^{-1} is achieved at a current density of 1.5 C (435 mA g^{-1}) (Fig. S26). Moreover, the Zn||PNZ battery exhibits an impressive cycling stability and maintains 100 mAh g^{-1} discharge capacity after 100 times at $-70\text{ }^{\circ}\text{C}$ (Fig. S27).

4 Conclusions

In summary, an aqueous-Mg(ClO₄)₂/Zn(ClO₄)₂ hydrates EDS electrolyte is reported and used for low-temperature AZIBs. Theoretical calculations and spectroscopic studies confirm the synergistic effect of cation and anion on freezing point reduction. Where Mg²⁺ acts as HBs donor bonding O atom in H₂O through strong electrostatic attraction to form stable hydration ions. And ClO₄⁻ as HBs acceptor can form weak HBs with H atom in H₂O. By simultaneously regulating the chemical environment of O and H atoms in H₂O, the 3.5 M Mg(ClO₄)₂ + 1 M Zn(ClO₄)₂ (3.5 M) obtains an ultralow freezing point of -121 °C, high ionic conductivity of 1.41 mS cm⁻¹ (-70 °C) and low viscosity of 22.9 mPa s (-70 °C). Based on significant anti-freezing characteristic of 3.5 M electrolyte, organic small molecules PTO and PNZ are developed to fabricate low-temperature AZIBs. Especially, the Zn||PTO battery delivers a high discharge capacity (101.5 mAh g⁻¹ at 0.5 C), excellent rate performance (71 mAh g⁻¹ at 3 C), and cycling stability (cycles 100 times with no obvious fading) at -70 °C. This work highlights the design of low-temperature aqueous electrolyte and promotes the development of low-temperature AZIBs.

Acknowledgements This study was supported the National Natural Science Foundation of China (51771094 and 21835004), Ministry of Education of China (B12015), and Tianjin Natural Science Foundation (18JCZDJC31500).

Open Access This article is licensed under a Creative Commons Attribution 4.0 International License, which permits use, sharing, adaptation, distribution and reproduction in any medium or format, as long as you give appropriate credit to the original author(s) and the source, provide a link to the Creative Commons licence, and indicate if changes were made. The images or other third party material in this article are included in the article's Creative Commons licence, unless indicated otherwise in a credit line to the material. If material is not included in the article's Creative Commons licence and your intended use is not permitted by statutory regulation or exceeds the permitted use, you will need to obtain permission directly from the copyright holder. To view a copy of this licence, visit <http://creativecommons.org/licenses/by/4.0/>.

Supplementary Information The online version contains supplementary material available at <https://doi.org/10.1007/s40820-021-00733-0>.

References

1. Z. Tie, L. Liu, S. Deng, D. Zhao, Z. Niu, Proton insertion chemistry of a zinc-organic battery. *Angew. Chem. Int. Ed.* **59**, 4920–4924 (2020). <https://doi.org/10.1002/anie.201916529>
2. K. Zhu, T. Wu, K. Huang, NaCa_{0.6}V₆O₁₆·3H₂O as an ultra-stable cathode for Zn-ion batteries: the roles of pre-inserted dual-cations and structural water in V₃O₈ layer. *Adv. Energy Mater.* **9**, 1901968 (2019). <https://doi.org/10.1002/aenm.201901968>
3. X. Yuan, T. Sun, S. Zheng, J. Bao, J. Liang et al., An inverse-spinel Mg₂MnO₄ cathode for high-performance and flexible aqueous zinc-ion batteries. *J. Mater. Chem. A* **8**, 22686–22693 (2020). <https://doi.org/10.1039/d0ta08916h>
4. K.W. Nam, H. Kim, Y. Beldjoudi, T.W. Kwon, D.J. Kim et al., Redox-active phenanthrenequinone triangles in aqueous rechargeable zinc batteries. *J. Am. Chem. Soc.* **142**, 2541–2548 (2020). <https://doi.org/10.1021/jacs.9b12436>
5. J. Hao, X. Li, X. Zeng, D. Li, J. Mao et al., Deeply understanding the Zn anode behaviour and corresponding improvement strategies in different aqueous Zn-based batteries. *Energy Environ. Sci.* **13**, 3917–3949 (2020). <https://doi.org/10.1039/d0ee02162h>
6. J. Hao, J. Long, B. Li, X. Li, S. Zhang et al., Toward high-performance hybrid Zn-based batteries via deeply understanding their mechanism and using electrolyte additive. *Adv. Funct. Mater.* **29**, 1903605 (2019). <https://doi.org/10.1002/adfm.201903605>
7. C.X. Zhao, J.N. Liu, N. Yao, J. Wang, D. Ren et al., Can aqueous zinc-air batteries work at sub-zero temperatures? *Angew. Chem. Int. Ed.* **60**, 15281–15285 (2021). <https://doi.org/10.1002/anie.202104171>
8. Q. Zhang, K.X. Xia, Y.L. Ma, Y. Lu, L. Li et al., Chaotropic anion and fast-kinetics cathode enabling low-temperature aqueous Zn batteries. *ACS Energy Lett.* **6**, 2704–2712 (2021). <https://doi.org/10.1021/acseenergylett.1c01054>
9. Q. Zhang, Y.L. Ma, Y. Lu, L. Li, F. Wan et al., Modulating electrolyte structure for ultralow temperature aqueous zinc batteries. *Nat. Commun.* **11**, 4463 (2020). <https://doi.org/10.1038/s41467-020-18284-0>
10. T.J. Sun, H.H. Du, S.B. Zheng, J.Q. Shi, Z.L. Tao, High power and energy density aqueous proton battery operated at -90 °C. *Adv. Funct. Mater.* **31**, 2010127 (2021). <https://doi.org/10.1002/adfm.202010127>
11. Q. Nian, J. Wang, S. Liu, T. Sun, S. Zheng et al., Aqueous batteries operated at -50 °C. *Angew. Chem. Int. Ed.* **58**, 16994–16999 (2019). <https://doi.org/10.1002/anie.201908913>
12. J. Hao, L. Yuan, C. Ye, D. Chao, K. Davey et al., Boosting zinc electrode reversibility in aqueous electrolytes by using low-cost antisolvents. *Angew. Chem. Int. Ed.* **60**, 7366–7375 (2021). <https://doi.org/10.1002/anie.202016531>
13. M. Becker, R.S. Kuhnel, C. Battaglia, Water-in-salt electrolytes for aqueous lithium-ion batteries with liquidus temperatures below -10 °C. *Chem. Commun.* **55**, 12032–12035 (2019). <https://doi.org/10.1039/c9cc04495g>



14. L. Jiang, Y. Lu, C. Zhao, L. Liu, J. Zhang et al., Building aqueous K-ion batteries for energy storage. *Nat. Energy* **4**, 495–503 (2019). <https://doi.org/10.1038/s41560-019-0388-0>
15. Z. Pei, Z. Yuan, C. Wang, S. Zhao, J. Fei et al., A flexible rechargeable zinc-air battery with excellent low-temperature adaptability. *Angew. Chem. Int. Ed.* **59**, 4793–4799 (2020). <https://doi.org/10.1002/anie.201915836>
16. C. Lu, X. Chen, All-temperature flexible supercapacitors enabled by antifreezing and thermally stable hydrogel electrolyte. *Nano Lett.* **20**, 1907–1914 (2020). <https://doi.org/10.1021/acs.nanolett.9b05148>
17. J.W. Zhao, J. Zhang, W.H. Yang, B.B. Chen, Z.M. Zhao et al., “Water-in-deep eutectic solvent” electrolytes enable zinc metal anodes for rechargeable aqueous batteries. *Nano Energy* **57**, 625–634 (2019). <https://doi.org/10.1016/j.nanoen.2018.12.086>
18. W. Yang, X. Du, J. Zhao, Z. Chen, J. Li et al., Hydrated eutectic electrolytes with ligand-oriented solvation shells for long-cycling zinc-organic batteries. *Joule* **4**, 1557–1574 (2020). <https://doi.org/10.1016/j.joule.2020.05.018>
19. J. Shi, T. Sun, J. Bao, S. Zheng, H. Du et al., “Water-in-deep eutectic solvent” electrolytes for high-performance aqueous Zn-ion batteries. *Adv. Funct. Mater.* **31**, 2102035 (2021). <https://doi.org/10.1002/adfm.202102035>
20. X. Bu, Y. Zhang, Y. Sun, L. Su, J. Meng et al., All-climate aqueous supercapacitor enabled by a deep eutectic solvent electrolyte based on salt hydrate. *J. Energy Chem.* **49**, 198–204 (2020). <https://doi.org/10.1016/j.jechem.2020.02.042>
21. Y. Marcus, Unconventional deep eutectic solvents: aqueous salt hydrates. *ACS Sustain. Chem. Eng.* **5**, 11780–11787 (2017). <https://doi.org/10.1021/acssuschemeng.7b03528>
22. T. Sun, X. Yuan, K. Wang, S. Zheng, J. Shi et al., An ultralow-temperature aqueous zinc-ion battery. *J. Mater. Chem. A* **9**, 7042–7047 (2021). <https://doi.org/10.1039/d0ta12409e>
23. L. Cao, D. Li, F.A. Soto, V. Ponce, B. Zhang et al., Highly reversible aqueous zinc batteries enabled by zincophilic-zincophobic interfacial layers and interrupted hydrogen-bond electrolytes. *Angew. Chem. Int. Ed.* **60**, 18845–18851 (2021). <https://doi.org/10.1002/anie.202107378>
24. Y. Sun, H. Ma, X. Zhang, B. Liu, L. Liu et al., Salty ice electrolyte with superior ionic conductivity towards low-temperature aqueous zinc ion hybrid capacitors. *Adv. Funct. Mater.* **31**, 2101277 (2021). <https://doi.org/10.1002/adfm.202101277>
25. K. Nieszporek, J. Nieszporek, Multi-centred hydrogen bonds between water and perchlorate anion. *Phys. Chem. Liq.* **55**, 473–481 (2016). <https://doi.org/10.1080/00319104.2016.1227811>
26. K. Nieszporek, P. Podkoscielny, J. Nieszporek, Transitional hydrogen bonds in aqueous perchlorate solution. *Phys. Chem. Chem. Phys.* **18**, 5957–5963 (2016). <https://doi.org/10.1039/c5cp07831h>
27. B. Tansel, J. Sager, T. Rector, J. Garland, R.F. Strayer et al., Significance of hydrated radius and hydration shells on ionic permeability during nanofiltration in dead end and cross flow modes. *Sep. Purif. Technol.* **51**, 40–47 (2006). <https://doi.org/10.1016/j.seppur.2005.12.020>
28. F. David, V. Vokhminz, G. Ionova, Water characteristics depend on the ionic environment. Thermodynamics and modelisation of the aquo ions. *J. Mol. Liq.* **90**, 45–62 (2001). [https://doi.org/10.1016/S0167-7322\(01\)00106-4](https://doi.org/10.1016/S0167-7322(01)00106-4)
29. M. Śmiechowski, J. Stangret, ATR FT-IR H₂O spectra of acidic aqueous solutions. Insights about proton hydration. *J. Mol. Struct.* **878**, 104–115 (2008). <https://doi.org/10.1016/j.molstruc.2007.08.001>
30. Y. Chen, Y.-H. Zhang, L.-J. Zhao, ATR-FTIR spectroscopic studies on aqueous LiClO₄, NaClO₄, and Mg(ClO₄)₂ solutions. *Phys. Chem. Chem. Phys.* **6**, 537–542 (2004). <https://doi.org/10.1039/b311768e>
31. Z. Dou, L. Wang, J. Hu, W. Fang, C. Sun et al., Hydrogen bonding effect on Raman modes of formic acid-water binary solutions. *J. Mol. Liq.* **313**, 113595 (2020). <https://doi.org/10.1016/j.molliq.2020.113595>
32. S.L. Simon, Temperature-modulated differential scanning calorimetry: theory and application. *Thermochim. Acta* **374**, 55–71 (2001). [https://doi.org/10.1016/S0040-6031\(01\)00493-2](https://doi.org/10.1016/S0040-6031(01)00493-2)
33. F. Wan, L. Zhang, X. Dai, X. Wang, Z. Niu et al., Aqueous rechargeable zinc/sodium vanadate batteries with enhanced performance from simultaneous insertion of dual carriers. *Nat. Commun.* **9**, 1656 (2018). <https://doi.org/10.1038/s41467-018-04060-8>
34. M. Zhu, X. Wang, H. Tang, J. Wang, Q. Hao et al., Antifreezing hydrogel with high zinc reversibility for flexible and durable aqueous batteries by cooperative hydrated cations. *Adv. Funct. Mater.* **30**, 1907218 (2019). <https://doi.org/10.1002/adfm.201907218>
35. P. Wang, X. Xie, Z. Xing, X. Chen, G. Fang et al., Mechanistic insights of Mg²⁺-electrolyte additive for high-energy and long-life zinc-ion hybrid capacitors. *Adv. Energy Mater.* **11**, 2102258 (2021). <https://doi.org/10.1002/aenm.202101158>
36. T. Sun, C. Liu, X. Xu, Q. Nian, S. Zheng et al., Insights into the hydronium-ion storage of alloxazine in mild electrolyte. *J. Mater. Chem. A* **8**, 21983–21987 (2020). <https://doi.org/10.1039/d0ta09316e>
37. Z. Guo, J. Huang, X. Dong, Y. Xia, L. Yan et al., An organic/inorganic electrode-based hydronium-ion battery. *Nat. Commun.* **11**, 959 (2020). <https://doi.org/10.1038/s41467-020-14748-5>
38. T. Sun, C. Liu, J. Wang, Q. Nian, Y. Feng et al., A phenazine anode for high-performance aqueous rechargeable batteries in a wide temperature range. *Nano Res.* **13**, 676–683 (2020). <https://doi.org/10.1007/s12274-020-2674-3>
39. J. Hong, M. Lee, B. Lee, D.-H. Seo, C.B. Park et al., Biologically inspired pteridine redox centres for rechargeable batteries. *Nat. Commun.* **5**, 5335 (2014). <https://doi.org/10.1038/ncomms6335>